PHYSICAL REVIEW APPLIED **18,** 034035 (2022)

High-Sensitivity Air-Coupled Megahertz-Frequency Ultrasound Detection Using On-Chip Microcavities

Hao Yang,[1,2] Zhi-Gang Hu,[1,2] Yuechen Lei,[1,2] Xuening Cao,[1,2] Min Wang,[1,2] Jialve Sun,[3]
Zhanchun Zuo,[1,4] Changhui Li,[3] Xiulai Xu,[1] and Bei-Bei Li[1,4,*]

[1] *Beijing National Laboratory for Condensed Matter Physics, Institute of Physics, Chinese Academy of Sciences, Beijing 100190, China*
[2] *University of Chinese Academy of Sciences, Beijing 100049, China*
[3] *College of Future Technology, Peking University, Beijing 100871, China*
[4] *Songshan Lake Materials Laboratory, Dongguan, Guangdong 523808, China*

(Received 11 March 2022; revised 21 May 2022; accepted 4 August 2022; published 14 September 2022; corrected 16 November 2022)

Owing to their dual-resonance enhanced sensitivity, cavity optomechanical systems provide an ideal platform for ultrasound sensing. In this work, we realize high-sensitivity air-coupled ultrasound sensing from kilohertz to megahertz frequency range based on whispering gallery mode microcavities. Using a 57-μm-diameter microtoroid with high optical Q factor (approximately 10^7) and mechanical Q factor (approximately 700), we achieve sensitivities of 46 $\mu\text{Pa}\,\text{Hz}^{-1/2}$–10 $\text{mPa}\,\text{Hz}^{-1/2}$ in a frequency range of 0.25–3.2 MHz. Thermal-noise-limited sensitivity is realized around a mechanical resonance at 2.56 MHz, in a frequency range of 0.6 MHz. We also observe the second- and third-order mechanical sidebands, and quantitatively study the intensities of each mechanical sideband as a function of the mechanical displacement. Measuring the combination of signal-to-noise ratios at all sidebands has the potential to extend the dynamic range of ultrasound sensing.

DOI: 10.1103/PhysRevApplied.18.034035

I. INTRODUCTION

Miniaturized high-sensitivity ultrasound sensors are key components in various applications, such as medical diagnostics [1], photoacoustic imaging and spectroscopy [2–4], nondestructive testing [5], sonar [6,7], trace gas monitoring [8], etc. Currently, piezoelectric transducers are most widely used, but their sensitivities drop quickly when the size becomes smaller, leading to a typical sensor size of millimeter to centimeter scale [9–11]. In order to realize both high sensitivity and spatial resolution, photonic ultrasound sensors that can be microfabricated on a silicon chip have been developed. Among them, cavity optomechanical systems [12–15] are attracting increasing interest owing to their superior characteristics of high sensitivity, broad bandwidth, low power consumption, and chip-scale integration. In cavity optomechanical systems, displacement of the cavity can be optically read out via optomechanical coupling. As the response is enhanced by mechanical resonance, and the readout sensitivity can be also enhanced by optical resonance, cavity optomechanical systems have been found to be an ideal sensing platform for displacement [16,17], mass [18–20], force [21–23], acceleration [24,25], magnetic field [26–32], acoustic waves [33–48], etc.

Ultrasound sensing using cavity optomechanical systems in a liquid environment has been demonstrated with various microcavity systems. Polymer materials are generally soft and can be easily deformed by acoustic waves, and therefore provide large sensing signals. Various polymer microcavities, such as those of polystyrene [33,34], SU8 [35], and polydimethylsiloxane [36], have been fabricated for ultrasound sensing, and achieved sensitivity at the pascal level and high bandwidth of tens to hundreds of megahertz. A Fabry-Perot cavity has been fabricated at the end of an optical fiber using UV-curable epoxy, which realized a sensitivity of $\text{mPa}\,\text{Hz}^{-1/2}$ at the tens of megahertz frequency range [37]. Silicon microcavities have also attracted increasing interest, as they can be mass produced on a chip and their fabrication techniques have been well developed in the past few decades. Recently, Shnaiderman *et al.* demonstrated miniaturized high-sensitivity ultrasound sensing using an array of pointlike silicon waveguide-etalon detectors on a silicon-on-insulator platform, and realized a sensing bandwidth of hundreds of megahertz [38]. Later, Westerveld *et al.* demonstrated an

---

[*] libeibei@iphy.ac.cn

optomechanical ultrasound sensor using a silicon microring cavity coupled with a thin film, with a 15-nm gap in between, and realized a sensitivity of mPa $\mathrm{Hz}^{-1/2}$ in the tens of megahertz frequency range [39]. Silica microcavities have also been extensively explored for ultrasound sensing, due to their ultrahigh optical Q factors. Ultrasound sensing in a liquid environment has been demonstrated using microtoroid [40,41] and microsphere [34,42] cavities.

Air-coupled ultrasound sensing has specific applications such as gas photoacoustic spectroscopy [49] and noncontact ultrasonic medical imaging [50]. Due to the large impedance mismatch at the acoustic source/air interface and the absorption loss of ultrasonic waves, air-coupled ultrasound detection requires ultrahigh sensitivity. Ultrasound sensing in air has been demonstrated using microbottle cavities, with sensitivities of the order of mPa $\mathrm{Hz}^{-1/2}$ at tens to hundreds of kilohertz frequency range [43,44]. Through detecting the acoustic-wave-induced modulation of a Brillouin laser in a microsphere, acoustic sensitivity of 267 μPa $\mathrm{Hz}^{-1/2}$ has been realized in the kilohertz frequency range [45]. Basiri-Esfahani *et al.* have realized ultrasound sensing in the thermal-noise-dominant regime using a spoked microdisk cavity, and achieved sensitivities of 8–300 μPa $\mathrm{Hz}^{-1/2}$ in the frequency range from 1 kHz to 1 MHz [46]. Up to now, high-sensitivity ultrasound sensing in air above 1 MHz has not been reported.

In this work, we demonstrate air-coupled ultrasound detection in the megahertz frequency range. To extend the sensing frequency into the megahertz range, we use a microtoroid with a diameter of 57 μm, which supports mechanical resonances in the megahertz range. To decrease the constraint of the mechanical motion from the substrate, we use a two-step etching process to make a microtoroid with a thin silicon pedestal. This allows a high mechanical Q factor of approximately 700 of the first-order flapping mode at 2.56 MHz. Compared with the spoked microdisk used in Ref. [46], the microtoroid has less squeeze-film damping due to the larger allowed undercut (distance between toroid and substrate). Combining with the high optical Q factor of approximately 10^7, thermal-noise-limited sensitivity is reached in air, within a frequency range of 0.6 MHz. We achieve sensitivities of 46 μPa $\mathrm{Hz}^{-1/2}$–10 mPa $\mathrm{Hz}^{-1/2}$ in the frequency range of 0.25–3.2 MHz. We also observe second- and third-order mechanical sidebands in the noise power spectrum, when driving the sensor with an ultrasonic wave at mechanical resonance, which is caused by the transduction nonlinearity. We measure the signal-to-noise ratios (SNRs) under different ultrasound pressures (P), and find that $\sqrt{\mathrm{SNR}}$s of the first-, second-, and third-order mechanical sidebands are approximately proportional to P, P^2, and P^3, respectively, which agree well with our theoretical results.

II. METHODS

The ultrasound sensitivity is determined by the noise of the sensor. In our detection system, the main sources of noise are laser noise from the probe light and mechanical thermal noise from the nonzero temperature environment. The laser noise mainly consists of classical noise (including intensity noise and phase noise), which is the dominant noise source in the low-frequency range, and quantum shot noise, which is dominant at high frequencies. For a microcavity with optical energy decay rate of κ and mechanical damping rate of γ, the corresponding noise equivalent pressure, i.e., the ultrasound sensitivity $P_{\min}$, can be expressed as Eq. (1) [13,46]:

$$
\begin{aligned}
P_{\min}(\omega) &= \frac{1}{r\zeta A}\sqrt{\frac{S_{xx}^{\mathrm{shot}}+S_{xx}^{\mathrm{classical}}}{|\chi_m|^2}+S_{FF}^{\mathrm{thermal}}} \\
&= \frac{1}{r\zeta A}\sqrt{\frac{\frac{\kappa(1+4\omega^2/\kappa^2)}{16\eta n_c G^2}+S_{xx}^{\mathrm{classical}}}{|\chi_m|^2}+2m\gamma k_B T}, \quad (1)
\end{aligned}
$$

where r is the ratio of the pressure difference between the upper and lower surfaces of the device to the peak pressure at the antinode of the ultrasonic wave, as the cavity only moves by feeling the pressure difference between the upper and lower surfaces, ζ is the spatial overlap between the incident ultrasound and the mechanical displacement profile of the sensor, ω is the angular frequency of the incident ultrasonic wave, and A is the sensor area. The first term under the square root denotes the optical noise, with S_{xx}^{shot} and $S_{xx}^{\mathrm{classical}}$ representing displacement power spectral densities of shot noise [51] and classical noise, respectively. η is the total detection efficiency of light, and n_{c} is the number of photons in the cavity. $G = d\omega/dx$ denotes the optomechanical coupling coefficient, quantifying the cavity frequency shift for unit mechanical displacement x. The second term under the square root quantifies thermal noise at temperature T, introduced by both the intrinsic damping of the mechanical resonator and collisions with the gas molecules around the sensor. Here m is the effective mass of the sensor and $\chi_m(\omega)$ is the mechanical susceptibility, quantified by $\chi_m(\omega) = 1/m(\Omega^2 - \omega^2 - i\gamma\omega)$, with Ω being the angular frequency of the mechanical resonance. From Eq. (1), we can see that the sensitivity is fundamentally limited by the thermal noise, if the measurement strength is strong enough to enable thermal noise to dominate laser noise. As a result, reaching the thermal-noise-limited regime is beneficial to achieving better sensitivity. This can be realized by increasing the optical Q factor, mechanical Q factor, and optomechanical coupling coefficient G. A larger sensing bandwidth can be obtained by increasing the thermal-noise-dominant frequency range.

The first-order flapping mode has a large spatial overlap with the ultrasonic wave coming from the top of the sensor, which is beneficial to achieving good ultrasound sensitivity. We then optimize the ultrasound sensitivity for this mode, by changing the geometric parameters of the toroid. We first simulate the resonance frequency for different principal diameters of the cavity from 30 to 1000 μm, with the result shown in Fig. 1(a). In the simulation, we keep the minor diameter of the toroid to be 6 μm and the disk thickness to be 2 μm. It can be seen that, with an increase of the principal diameter, the resonance frequency decreases monotonically. Thus, for ultrasound sensing at high frequency, a microcavity with a smaller diameter (and therefore higher mechanical frequency) is desired. We then calculate the thermal-noise-limited ultrasound sensitivity for different principal diameters of the toroid, as shown in Fig. 1(b). In the calculation, we use the mechanical Q factor of $Q_m = 700$, obtained from our experiment. It can be seen that with an increase of the principal diameter, the sensitivity gets better, due to the increased sensing area. For low-frequency ultrasound sensing, using a cavity with a larger diameter is beneficial to achieving better sensitivity. We then simulate the resonance frequency and calculate the corresponding thermal-noise-limited sensitivity for different disk thicknesses from 200 nm to 5 μm, as shown in Figs. 1(c) and 1(d), respectively. It can be seen that, with the disk thickness increasing, the resonance frequency increases, and the sensitivity gets worse.

In our experiment, in order to facilitate the fabrication of a high-optical-Q toroid, we choose the disk thickness to be 2 μm instead of a thinner one. In order to optimize the ultrasound sensitivity at megahertz frequency range, we use a toroid with a principal (minor) diameter of approximately 57 (6) μm, whose mechanical resonance frequency of the first-order flapping mode is approximately 2.56 MHz and corresponding effective mass is $m = 12.1$ ng. For an ideal case, $\zeta = 1$, $r = 1$, and the corresponding sensitivity is calculated to be approximately 18.5 $\mu\text{Pa Hz}^{-1/2}$.

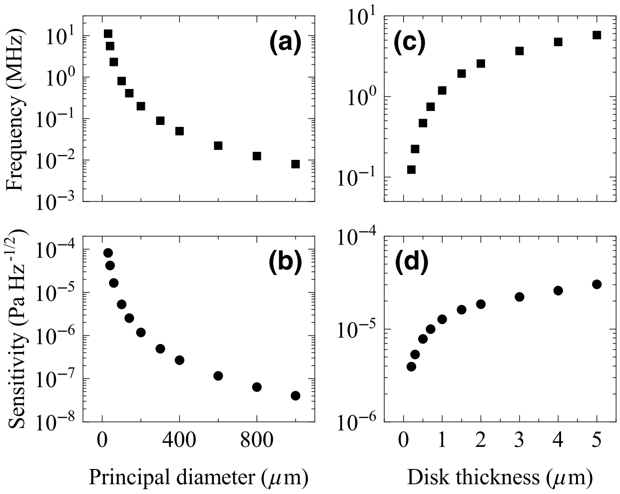

FIG. 1. (a) Simulated mechanical resonance frequency and (b) calculated sensitivity of the sensor, with different principal diameters. (c) Simulated mechanical resonance frequency and (d) calculated sensitivity of the sensor, with different disk thicknesses.

The microtoroid cavity is fabricated by standard microfabrication processes [52] from a silica-on-silicon wafer, including photolithography, hydrofluoric acid wet etching, xenon difluoride (XeF_2) dry etching, and a CO_2 laser reflow process. After the reflow process, we perform a second XeF_2 dry etching to obtain a thin silicon pedestal of approximately 5 μm in diameter. This can increase its mechanical compliance and decrease the mechanical energy dissipation from the cavity to the substrate, and therefore enable higher mechanical Q factor. Figure 2(a) shows a top-view optical microscope image of the microtoroid. Figure 2(b) is the finite-element-method (FEM)-simulated optical field distribution of the fundamental whispering gallery mode (WGM) of the microtoroid, where the optical field is confined around the periphery of the microcavity. The measured transmission spectrum for one WGM of the microtoroid approximately 1550 nm is shown in Fig. 2(c). We can see a mode splitting for the microtoroid, which is caused by the backscattering from the surface roughness of the cavity. From the double-peak Lorentzian fitting of the transmission spectrum (the red curve), we can derive the intrinsic optical Q factor to be about 10^7. The optical Q factor allows a 3-dB bandwidth of 16.8 MHz, considering the frequency dependence of the shot noise [Eq. (1)].

The measurement setup for ultrasound sensing using the microtoroid is shown in Fig. 2(d), with a scanning electron microscope (SEM) image of the microtoroid included. Light from a tunable narrow-linewidth fiber laser in the 1550-nm wavelength band is coupled into the WGMs of the toroid through a tapered fiber [53]. The transmitted light from the tapered fiber is detected by a photodetector, and monitored by an oscilloscope to obtain the transmission spectrum. The principle of ultrasound detection is shown in the inset of Fig. 2(d). When an ultrasonic wave is applied to the sensor, it can drive the mechanical motion of the cavity and induce a change in the cavity circumference or the taper-cavity coupling strength. Both translate into an amplitude modulation of the intracavity field, which can be optically read out. In our experiment, we use a proportional-integral-derivative controller to lock the laser wavelength on the side of the optical mode with a detuning where the transmission has the largest slope, to optimize the dispersive transduction of ultrasound signal. The mechanical spectrum of the toroid is measured with an electronic spectrum analyzer (ESA). The ultrasound signal is produced by an ultrasonic transducer. For experimental convenience, the angle between the incident ultrasound and the disk surface is kept to be approximately 30°.

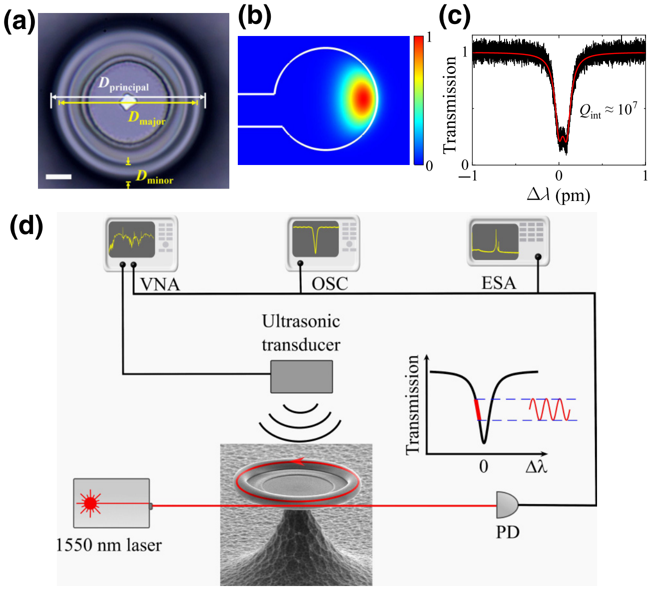

FIG. 2. (a) Top-view optical microscope image of the microtoroid. $D_{\mathrm{principal}}$, D_{major}, and D_{minor} denote the principal, major, and minor diameters of the microtoroid, with $D_{\mathrm{principal}} = D_{\mathrm{major}} + D_{\mathrm{minor}}$. The scale bar corresponds to 10 μm. (b) Simulated optical field intensity distribution of the fundamental WGM of the microtoroid, normalized to its maximum value. (c) Measured transmission spectrum (black solid curve) of the microtoroid around 1550 nm, with the red solid curve showing the double Lorentzian fitting result, from which we can obtain $Q_{\mathrm{int}} \approx 10^7$. (d) Schematic diagram of the experimental setup for ultrasound sensing, with the inset showing the principle of ultrasound detection. PD, photodetector; VNA, vector network analyzer; OSC, oscilloscope; ESA, electronic spectrum analyzer. A SEM image of the microtoroid is shown in the setup.

We use a function generator to apply a single-frequency sinusoidal voltage to the transducer to measure the single-frequency response of the sensor, and use a vector network analyzer to sweep the frequency of the applied ultrasonic wave to obtain the system response of the ultrasound sensor.

To obtain the sensitivity in a broad frequency range, two piezoelectric ultrasonic transducers with center frequencies at 1 and 5 MHz are used. Considering the attenuation of ultrasonic waves in air, the relation between the ultrasound pressure at the sensor (P_{sensor}) and that at the ultrasonic transducer (P_{PZT}) is $P_{\mathrm{sensor}}(\omega) = e^{-\alpha(\omega)d} P_{\mathrm{PZT}}(\omega)$, where d is the distance between the ultrasonic transducer and the sensor, which is kept to be approximately 1 cm in our experiment. $\alpha(\omega)$ is the frequency-dependent acoustic attenuation coefficient, which is obtained from the Stokes-Kirchhoff formula [54,55]:

$$\alpha(\omega) = \frac{\omega^2}{2\rho v^3}\left[\frac{4}{3}\eta' + \left(\frac{1}{C_v} - \frac{1}{C_p}\right)\right], \qquad (2)$$

where ρ is the density, v is the speed of sound, η' is the dynamic viscosity coefficient, and C_v and C_p are the specific heat capacities at constant volume and constant pressure, respectively. From this formula, we can see that the absorption loss is proportional to the square of frequency. For example, α is 0.30 and 122 dB/cm for ultrasonic waves of 0.5 and 10 MHz, respectively. This frequency-dependent absorption loss makes high-frequency ultrasound sensing in air challenging. The generated ultrasound pressures at different frequencies are calibrated using a hydrophone. We measure the ultrasound pressure generated by the transducer in water at different frequencies with the hydrophone, and then derive the pressure in air, taking into account the acoustic impedance mismatch, $P_{\mathrm{air}} = P_{\mathrm{water}} Z_{\mathrm{air}}/Z_{\mathrm{water}} = P_{\mathrm{water}}/3580$, where $Z = \rho v$ is the acoustic impedance of the material.

III. RESULTS

We measure the ultrasound sensitivity of the microtoroid cavity. In order to enable a thermal-noise-limited sensing, but to avoid radiation-pressure-induced self-sustained mechanical oscillation [56,57], we keep the input power to be approximately 10 μW. At this input power, the laser noise is dominated by shot noise in the megahertz frequency range. The noise power spectrum measured with the ESA is shown as the black solid curve in Fig. 3(a), in which we can see a mechanical resonance at $\Omega/2\pi = 2.56$ MHz. This corresponds to the first-order flapping mode, with its mode profile shown in the inset. The thermal noise, shot noise, and total noise in the frequency range of 2–3.2 MHz, calculated from Eq. (1), are shown as the orange dashed, blue dotted, and red dash-dotted curves in Fig. 3(a). The corresponding displacement power spectral density (S_{xx}) of the sensor is shown on the right-hand axis of Fig. 3(a). From the linewidth of the resonance, we can obtain the mechanical Q factor of this mode to be approximately 700. Regarding the mechanical damping of the mode, we theoretically calculate the contribution from the gas damping, which consists of the drag force damping and squeeze-film damping [58]. The drag force damping rate is calculated to be $\gamma_{\mathrm{drag}} = \mu l_{\mathrm{drag}}/m = 561$ Hz, with $\mu = 1.8 \times 10^{-5}$ $\mathrm{kg\,m^{-1}\,s^{-1}}$ being the coefficient of viscosity and $l_{\mathrm{drag}} = 16r\sqrt{m/M} = 0.376$ mm is the geometry-dependent characteristic length, with $r = 28.5$ μm being the radius of the toroid. $m = 12.1$ ng is the effective mass and $M = 17.8$ ng is the real mass of the toroid. For the squeeze-film damping, the characteristic length $l_{\mathrm{squeeze}} = (3\pi r^4)/(2h^3)\sqrt{m/M} = 0.32$ mm, with $h = 20$ μm being the distance between the cavity disk and the substrate. Thus, the squeeze-film damping rate is $\gamma_{\mathrm{squeeze}} = \mu l_{\mathrm{squeeze}}/m = 482$ Hz. The measured mechanical damping rate of $\gamma_{\mathrm{meas}} = 2\pi \times 3.66$ kHz is much larger than both γ_{drag} and $\gamma_{\mathrm{squeeze}}$, and therefore we believe the

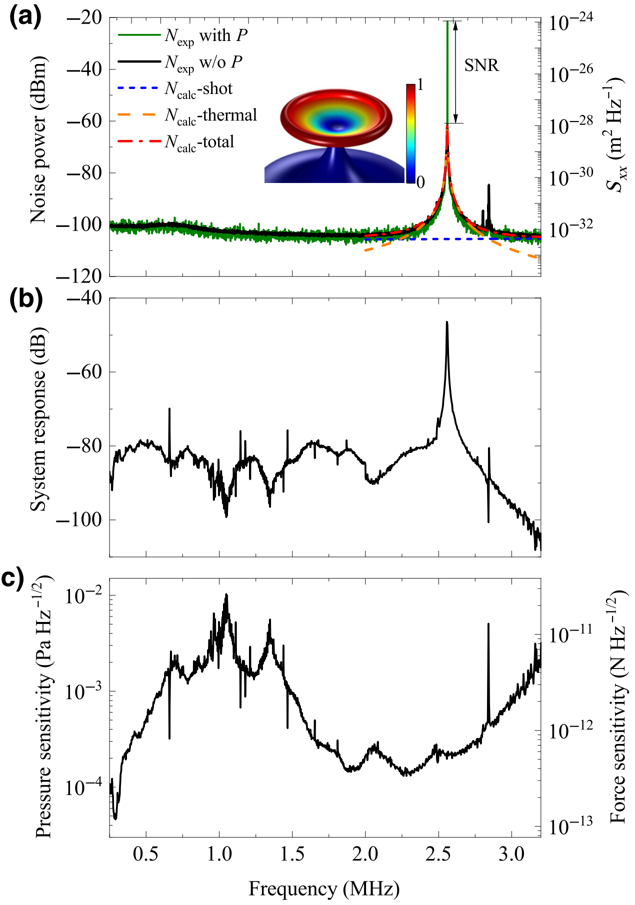

FIG. 3. (a) Noise power spectrum (black solid curve) and the response of the microtoroid (green solid curve) to ultrasound at 2.56 MHz, with a SNR of 41.39 dB. The orange dashed, blue dotted, and red dash-dotted curves are the calculated thermal noise, shot noise, and total noise, respectively, in the frequency range of 2–3.2 MHz. The inset shows the simulated displacement distribution of the first-order flapping mode, normalized to its maximum value. (b) System response of the microtoroid versus the ultrasound frequency. (c) Derived pressure (left axis) and force (right axis) sensitivity spectra of the microtoroid.

main damping rate of the microtoroid is induced by the intrinsic damping of the cavity structure.

When we apply an ultrasound signal with a pressure $P_{\rm applied} = 132.2$ mPa to the microtoroid sensor at 2.56 MHz, we obtain a SNR of 41.39 dB, measured with a resolution bandwidth $\Delta f = 20$ Hz, as shown as the green solid curve in Fig. 3(a). The sensitivity at 2.56 MHz can be calculated by the following equation:

$$P_{\rm min}(\Omega) = P_{\rm applied}(\Omega)\sqrt{\frac{1}{\rm SNR}\frac{1}{\Delta f}} \sim 252\ \mu{\rm Pa\,Hz}^{-1/2}. \tag{3}$$

Using the parameters in our experiment, the relative pressure difference ratio of the sensor is obtained to be $r = 1.17$ at 2.56 MHz, which is larger than 1, due to the substrate-reflection-enhanced ultrasound pressure at the microtoroid. Considering the incident angle $\theta = 30^\circ$ of the ultrasound, the spatial overlap ζ between the incident ultrasound and the first-order flapping mode of the microtoroid is 0.39. We can then derive the theoretical sensitivity at this frequency to be 41 μPa Hz$^{-1/2}$. The difference between the experimental and theoretical sensitivities could be a result of the misalignment of the ultrasonic transducer and the microtoroid sensor.

We then use a network analyzer to drive the ultrasonic transducer to obtain the system response of our sensor for ultrasonic waves with different frequencies. In order to obtain the sensor response in a broad frequency band, we use two ultrasonic transducers, with center frequencies at 1 and 5 MHz, respectively. System response in the frequency range of 0.25–3.2 MHz is obtained, as shown in Fig. 3(b). The lower frequency limit of 0.25 MHz is not intrinsic, but rather limited by the low pressure of the ultrasound produced by the transducer. The upper limit of 3.2 MHz is introduced by the larger attenuation of air at higher frequencies ($\alpha = 12.5$ dB/cm at 3.2 MHz). It can be seen that the response of the sensor around the resonance frequency of 2.56 MHz is significantly enhanced, due to the high mechanical Q factor of the mode and the large spatial overlap between the mode displacement and the ultrasonic wave. Other peaks in the frequency band correspond to other mechanical modes of the toroid or the tapered fiber. These modes do not reach the thermal-noise-dominant regime, and are therefore not seen in the noise power spectrum in Fig. 3(a).

From the system response $S(\omega)$ and the noise power spectral density $N(\omega)$, combined with the sensitivity $P_{\rm min}(\Omega)$ at $\Omega/2\pi = 2.56$ MHz, we can derive the sensitivity over the entire frequency range:

$$P_{\rm min}(\omega) = P_{\rm min}(\Omega)\frac{P_{\rm applied}(\omega)}{P_{\rm applied}(\Omega)}\sqrt{\frac{N(\omega)}{N(\Omega)}\frac{S(\Omega)}{S(\omega)}}, \tag{4}$$

where $P_{\rm applied}(\omega)$ is the applied ultrasound pressure to the sensor at different frequencies. The pressure sensitivity in the frequency range of 0.25–3.2 MHz is shown on the left-hand axis of Fig. 3(c). Multiplying the sensor area, we can obtain the force sensitivity of the sensor, as shown on the right-hand axis of Fig. 3(c). The achieved pressure (force) sensitivity is 46 μPa Hz$^{-1/2}$–10 mPa Hz$^{-1/2}$ (118 fN Hz$^{-1/2}$–26.4 pN Hz$^{-1/2}$) in the frequency range of 0.25–3.2 MHz. The peak sensitivity is achieved at 0.29 MHz where no mechanical mode of the toroid is shown from our simulated results. The sensitivity at this frequency could be enhanced by the mechanical resonance of the tapered fiber (see Appendix A for details). Around the mechanical resonance frequency, thermal-noise-limited pressure (force) sensitivity is reached of

130–475 μPa Hz$^{-1/2}$ (0.34–1.21 pN Hz$^{-1/2}$) in the frequency range of 2.24–2.84 MHz.

When we apply ultrasound at the mechanical resonance frequency $\Omega/2\pi = 2.56$ MHz, in addition to a response peak at 2.56 MHz, we also observe responses at the second- and third-order mechanical sidebands, as shown in Fig. 4(a). It can be seen that, when ultrasound pressure is applied, three peaks at Ω, 2Ω, and 3Ω frequencies appear in the noise power spectrum. At the input power of 10 μW, the radiation-pressure-force-induced mechanical oscillations can be neglected, and the higher-order mechanical sidebands are induced by nonlinear transduction. Since the cavity mode is a Lorentzian lineshape, the optical readout signal for displacement is a harmonic oscillation only for a small displacement. In the large-displacement case, the readout signal becomes anharmonic. Previous works have experimentally studied the intensities of the high-order mechanical sidebands as a function of the optical power [59–63] and theoretically studied the dependence of the high-order mechanical sidebands on the displacement [64]. Here we experimentally study the intensities of the high-order mechanical sidebands with different mechanical displacements, driven by an ultrasonic wave. Figure 4(b) shows the measured SNRs at the first-order (black squares), second-order (red circles), and third-order (blue triangles) sidebands. By performing exponential fittings to these experimental results, we obtain that $\sqrt{\mathrm{SNR}(\Omega)} \propto P^{1.13}$, $\sqrt{\mathrm{SNR}(2\Omega)} \propto P^{1.90}$, and $\sqrt{\mathrm{SNR}(3\Omega)} \propto P^{3.04}$. In the following we theoretically study the dependence of the SNR on the mechanical displacement at the three sidebands.

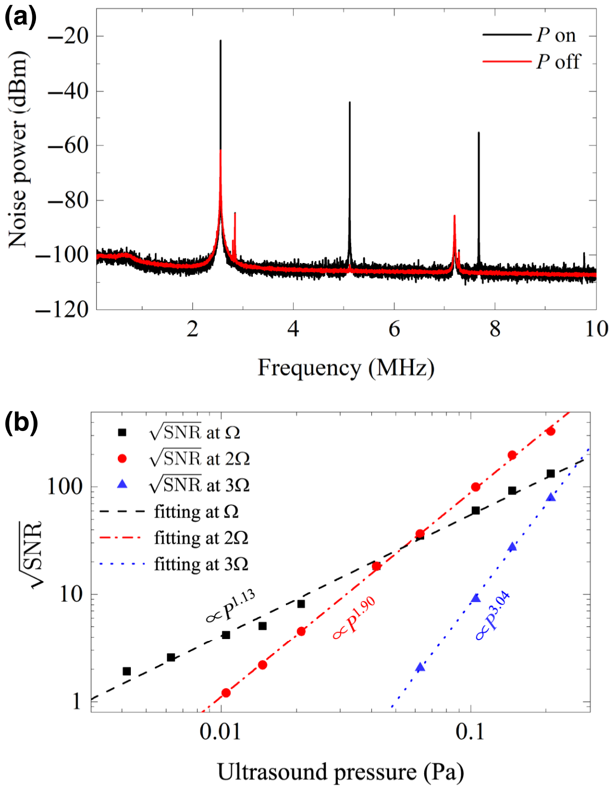

FIG. 4. (a) Noise power spectrum with (black curve) and without (red curve) applying a single-frequency ultrasound at 2.56 MHz. (b) $\sqrt{\mathrm{SNR}}$s versus ultrasound pressure at Ω (black squares), 2Ω (red circles), and 3Ω (blue triangles) frequencies, with the black dashed line, red dash-dotted line, and blue dotted line representing the corresponding fitting results.

From the equation of motion of the cavity mode $\dot{a} = -\kappa a/2 + i\Delta a + \sqrt{\kappa_e s}$, we can obtain the intracavity photon number to be $n_c = (4\kappa_e s/\kappa^2)[1/(1+\delta^2)]$, with s being the number of photons injected into the microcavity per unit time and $\kappa = \kappa_0 + \kappa_e$ being the total energy decay rate of the cavity mode. κ_0 is the intrinsic decay rate of the cavity mode and κ_e is the coupling rate with the tapered fiber. $\delta = 2\Delta/\kappa$ is the dimensionless detuning, with $\Delta = \omega - \omega_0$ denoting the frequency detuning between the input light and the cavity mode. Taylor-expanding the detuning δ, we can obtain the intracavity photon number to be

$$n_c \approx n_c^{\max}[c_0(\delta) + c_1(\delta)u + c_2(\delta)u^2 + c_3(\delta)u^3] \tag{5}$$

where $n_c^{\max}$ is the introcavity photon number when $\Delta = 0$, $c_0(\delta) = 1/(1+\delta^2)$, $c_n(\delta) = (1/i!)(d^i/d\delta^i)c_0(\delta)$. $u = 2Gx/\kappa$ represents the normalized frequency shift of the cavity mode caused by the mechanical displacement. Using the input-output relation $a_{\mathrm{out}} = \sqrt{s} - \sqrt{\kappa_e}a$, we can obtain the photocurrent arriving at the photodetector at a certain detuning:

$$Z = |a_{\mathrm{out}}|^2 \approx s - \frac{4\kappa_{\mathrm{e}}\kappa_0 s}{\kappa^2}\Bigg[c_0(\delta) + c_1(\delta)\frac{2G}{\kappa}x + c_2(\delta)\left(\frac{2G}{\kappa}\right)^2 x^2 + c_3(\delta)\left(\frac{2G}{\kappa}\right)^3 x^3\Bigg]. \tag{6}$$

Expressing the displacement of the cavity caused by the ultrasonic wave with $x = x_0\cos(\Omega t)$, we can obtain the following coefficients of the photocurrent for dc, Ω, 2Ω, and 3Ω frequency components:

$$Z_{\mathrm{dc}} = s - \frac{4\kappa_{\mathrm{e}}\kappa_0 s}{\kappa^2}c_0(\delta), \tag{7a}$$

$$Z_{\Omega} = -\frac{4\kappa_{\mathrm{e}}\kappa_0 s}{\kappa^2}c_1(\delta)\frac{2G}{\kappa}x_0\cos(\Omega\mathrm{t}), \tag{7b}$$

$$Z_{2\Omega} = -\frac{4\kappa_{\mathrm{e}}\kappa_0 s}{\kappa^2}\left[c_2(\delta)\left(\frac{2G}{\kappa}\right)^2\frac{x_0^2}{2}\cos(2\Omega\mathrm{t})\right], \tag{7c}$$

$$Z_{3\Omega} = -\frac{4\kappa_{\mathrm{e}}\kappa_0 s}{\kappa^2}\left[c_3(\delta)\left(\frac{2G}{\kappa}\right)^3\frac{x_0^3}{4}\cos(3\Omega\mathrm{t})\right]. \tag{7d}$$

As the amplitude of the mechanical displacement x_0 is proportional to the ultrasound pressure P, we can obtain the dependence of SNR on the ultrasound pressure P at the three mechanical sidebands, $\sqrt{\mathrm{SNR}}(\Omega) \propto P$, $\sqrt{\mathrm{SNR}}(2\Omega) \propto P^2$, and $\sqrt{\mathrm{SNR}}(3\Omega) \propto P^3$, respectively, which explains our experimental results well. Measuring the combination of SNRs at all the mechanical sidebands has the potential to extend the dynamic range of displacement sensing [59].

IV. CONCLUSIONS

We demonstrate air-coupled high-sensitivity megahertz-frequency ultrasound detection based on a microtoroid cavity with both high optical and mechanical Q factors. We extend the air-coupled ultrasound sensing into the megahertz frequency range, and achieve sensitivities of 46 μPa Hz$^{-1/2}$–10 mPa Hz$^{-1/2}$ in the frequency range of 0.25–3.2 MHz, with a thermal-noise-limited range of 0.6 MHz. In addition, we observe the second- and third-order mechanical sidebands when driving the sensor with ultrasound at the mechanical resonance frequency, and the measured intensities at three mechanical sidebands are consistent with our theoretical results. This nonlinear transduction provides a way to extend the dynamic range of displacement sensing.

The ultrasound sensitivity can be further improved by using a larger and thinner cavity, realizing a larger pressure difference ratio r by designing the structure, and optimizing the incident angle of the ultrasound. The use of mechanical modes with stronger optomechanical coupling coefficient [17] and squeezed light [31] can reduce shot noise and expand the thermal-noise-dominant regime. Integrated waveguide-coupled microcavities [65] and on-chip arrays of sensors can be designed in the future for photoacoustic imaging and spectroscopy [2–4]. This work broadens the frequency range of ultrasound detection in air, which is of great significance for applications in gas photoacoustic spectroscopy, noncontact ultrasonic medical imaging, etc. The photoacoustic signal near the resonance frequency has an enhanced response, which can be applied to high-sensitivity biomedical measurements [49,50].

ACKNOWLEDGMENTS

We are grateful for funding support from the National Key Research and Development Program of China (Grant No. 2021YFA1400700), the National Natural Science Foundation of China (NSFC) (Grants No. 91950118, No. 12174438, and No.11934019), and the Basic Frontier Science Research Program of Chinese Academy of Sciences (Grant No. ZDBS-LY-JSC003).

APPENDIX A

In Sec. III, we achieve a peak sensitivity of 46 μPa Hz$^{-1/2}$ at 0.29 MHz, where no mechanical mode of the microtoroid is shown from our simulated results. We infer that the sensitivity at this frequency is enhanced by a mechanical resonance of the tapered fiber, which has a large response to the ultrasound pressure and can be optically read out by the microcavity through dissipative optomechanical coupling between the taper and the cavity. The mechanical mode of the taper is not observed in

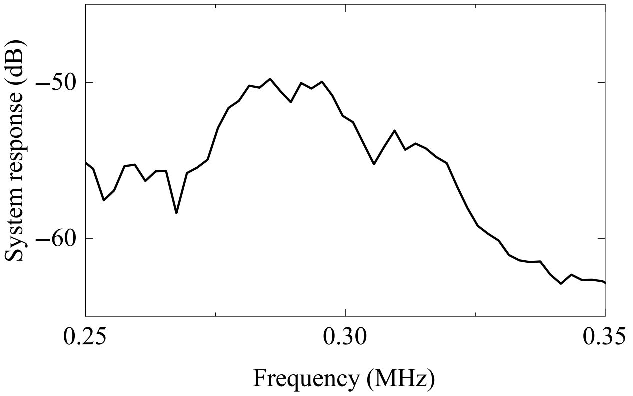

FIG. 5. Enlargement of system response of Fig. 3(b) in the main text, normalized by the ultrasound pressure of the transducer at different frequencies.

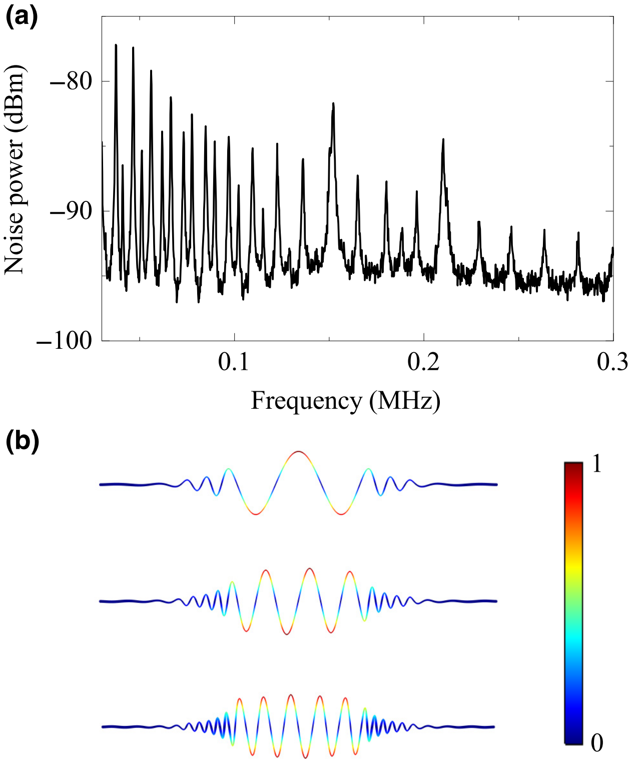

FIG. 6. (a) Noise power spectrum of the taper-microdisk coupled system, showing multiple mechanical resonances of the tapered fiber and the microdisk in the range of tens to hundreds of kilohertz. (b) The simulated normalized displacement distributions of the three taper modes at 90, 180, and 282 kHz.

the noise power spectrum in Fig. 3(a), because it does not reach the thermal-noise-limited regime, due to the weak optomechanical coupling between the taper and the microtoroid. Figure 5 is an enlargement of the system response of Fig. 3(b) in the main text, normalized by the ultrasound pressure of the transducer at different frequencies. We can see a peak response from 0.27 to 0.30 MHz, indicating a taper mode around this frequency.

To confirm this, we use a microdisk cavity with a wedge angle to measure the mechanical modes of the tapered fiber. The taper can be coupled with the microdisk from the wedge area. The mechanical motions of the tapered fiber induce a change in the gap between the tapered fiber and the disk, and therefore allow a strong dissipative coupling. As a result, the thermal mechanical motions of the tapered fiber can be optically read out. As shown in Fig. 6(a), several mechanical peaks appear in the noise power spectrum of the taper-microdisk coupled system, in the range of tens to hundreds of kilohertz. These resonance peaks correspond to the string modes of different orders of the tapered fiber and two disk modes (at 152 and 210 kHz). The mode profiles of three taper modes at 90, 180, and 282 kHz are shown in Fig. 6(b), obtained from FEM simulations.

[1] X. D. Wang, Y. J. Pang, G. Ku, X. Y. Xie, G. Stoica, and L. H. V. Wang, Noninvasive laser-induced photoacoustic tomography for structural and functional *in vivo* imaging of the brain, Nat. Biotechnol. **21**, 803 (2003).

[2] B. Dong, H. Li, Z. Zhang, K. Zhang, S. Chen, C. Sun, and H. F. Zhang, Isometric multimodal photoacoustic microscopy based on optically transparent micro-ring ultrasonic detection, Optica **2**, 169 (2015).

[3] T. Minamikawa, T. Masuoka, T. Ogura, K. Shibuya, R. Oe, E. Hase, Y. Nakajima, Y. Yamaoka, T. Mizuno, M. Yamagiwa, Y. Mizutani, H. Yamamoto, T. Iwata, K. Minoshima, and T. Yasui, Ultrasonic wave sensing using an optical-frequency-comb sensing cavity for photoacoustic imaging, OSA Contin. **2**, 439 (2019).

[4] J. T. Friedlein, E. Baumann, K. A. Briggman, G. M. Colacion, F. R. Giorgetta, A. M. Goldfain, D. I. Herman, E. V. Hoenig, J. Hwang, N. R. Newbury, E. F. Perez, C. S. Yung, I. Coddington, and K. C. Cossel, Dual-comb photoacoustic spectroscopy, Nat. Commun. **11**, 3152 (2020).

[5] B. Fischer, Optical microphone hears ultrasound, Nat. Photonics **10**, 356 (2016).

[6] M. P. Hayes and P. T. Gough, Synthetic aperture sonar: A review of current status, IEEE J. Ocean. Eng. **34**, 207 (2009).

[7] A. Elfes, Sonar-based real-world mapping and navigation, IEEE J. Robot. Autom. **3**, 249 (1987).

[8] H. Wu, L. Dong, H. Zheng, Y. Yu, W. Ma, L. Zhang, W. Yin, L. Xiao, S. Jia, and F. K. Tittel, Beat frequency quartz-enhanced photoacoustic spectroscopy for fast and calibration-free continuous trace-gas monitoring, Nat. Commun. **8**, 15331 (2017).

[9] B. W. Drinkwater and P. D. Wilcox, Ultrasonic arrays for non-destructive evaluation: A review, NDT E Int. **39**, 525 (2006).

[10] Z. Zhang, F. Li, R. Chen, T. Zhang, X. Cao, S. Zhang, T. R. Shrout, H. Zheng, K. K. Shung, M. S. Humayun, W. Qiu, and Q. Zhou, High-performance ultrasound needle transducer based on modified PMN-PT ceramic with ultrahigh clamped dielectric permittivity, IEEE T. Ultrason. Ferr. **65**, 223 (2018).

[11] T. Zheng, Y. Zhang, Q. Ke, H. Wu, L. W. Heng, D. Xiao, J. Zhu, S. J. Pennycook, K. Yao, and J. Wu, High-performance potassium sodium niobate piezoceramics for ultrasonic transducer, Nano Energy **70**, 104559 (2020).

[12] T. J. Kippenberg and K. J. Vahala, Cavity optomechanics: Back-action at the mesoscale, Science **321**, 1172 (2008).

[13] M. Aspelmeyer, T. J. Kippenberg, and F. Marquardt, Cavity optomechanics, Rev. Mod. Phys. **86**, 1391 (2014).

[14] M. Metcalfe, Applications of cavity optomechanics, Appl. Phys. Rev. **1**, 031105 (2014).

[15] B.-B. Li, L. Ou, Y. Lei, and Y.-C. Liu, Cavity optomechanical sensing, Nanophotonics **10**, 2799 (2021).

[16] B. P. Abbott, R. Abbott, T. D. Abbott, M. R. Abernathy, F. Acernese, K. Ackley, C. Adams, T. Adams, P. Addesso, and R. X. Adhikari *et al.*, Observation of Gravitational Waves from a Binary Black Hole Merger, Phys. Rev. Lett. **116**, 061102 (2016).

[17] A. Schliesser, G. Anetsberger, R. Rivière, O. Arcizet, and T. J. Kippenberg, High-sensitivity monitoring of micromechanical vibration using optical whispering gallery mode resonators, New J. Phys. **10**, 095015 (2008).

[18] W. Yu, W. C. Jiang, Q. Lin, and T. Lu, Cavity optomechanical spring sensing of single molecules, Nat. Commun. **7**, 12311 (2016).

[19] J.-J. Li and K.-D. Zhu, Nonlinear optical mass sensor with an optomechanical microresonator, Appl. Phys. Lett. **101**, 141905 (2012).

[20] F. Liu, S. Alaie, and Z. C. Leseman, and M. Hossein-Zadeh: Sub-pg mass sensing and measurement with an optomechanical oscillator, Opt. Express **21**, 19555 (2013).

[21] E. Gavartin, P. Verlot, and T. J. Kippenberg, A hybrid on-chip optomechanical transducer for ultrasensitive force measurements, Nat. Nanotechnol. **7**, 509 (2012).

[22] L. F. Buchmann, S. Schreppler, J. Kohler, N. Spethmann, and D. M. Stamper-Kurn, Complex Squeezing and Force Measurement Beyond the Standard Quantum Limit, Phys. Rev. Lett. **117**, 030801 (2016).

[23] S. Schreppler, N. Spethmann, N. Brahms, T. Botter, M. Barrios, and D. M. Stamper-Kurn, Optically measuring force near the standard quantum limit, Science **344**, 1486 (2014).

[24] A. G. Krause, M. Winger, T. D. Blasius, Q. Lin, and O. Painter, A high-resolution microchip optomechanical accelerometer, Nat. Photonics **6**, 768 (2012).

[25] F. Guzmán Cervantes, L. Kumanchik, J. Pratt, and J. M. Taylor, High sensitivity optomechanical reference accelerometer over 10 kHz, Appl. Phys. Lett. **104**, 221111 (2014).

[26] S. Forstner, S. Prams, J. Knittel, E. D. van Ooijen, J. D. Swaim, G. I. Harris, A. Szorkovszky, W. P. Bowen, and H. Rubinsztein-Dunlop, Cavity Optomechanical Magnetometer, Phys. Rev. Lett. **108**, 120801 (2012).

[27] S. Forstner, E. Sheridan, J. Knittel, C. L. Humphreys, G. A. Brawley, H. Rubinsztein-Dunlop, and W. P. Bowen, Ultrasensitive optomechanical magnetometry, Adv. Mater. **26,** 6348 (2014).

[28] C. Yu, J. Janousek, E. Sheridan, D. L. McAuslan, H. Rubinsztein-Dunlop, P. K. Lam, Y. Zhang, and W. P. Bowen, Optomechanical Magnetometry with a Macroscopic Resonator, Phys. Rev. Appl. **5,** 044007 (2016).

[29] J. Zhu, G. Zhao, I. Savukov, and L. Yang, Polymer encapsulated microcavity optomechanical magnetometer, Sci. Rep. **7,** 8896 (2017).

[30] B.-B. Li, D. Bulla, V. Prakash, S. Forstner, A. Dehghan-Manshadi, H. Rubinsztein-Dunlop, S. Foster, and W. P. Bowen, Invited article: Scalable high-sensitivity optomechanical magnetometers on a chip, APL Photonics **3,** 120806 (2018).

[31] B.-B. Li, J. Bílek, U. B. Hoff, L. S. Madsen, S. Forstner, V. Prakash, C. Schäfermeier, T. Gehring, W. P. Bowen, and U. L. Andersen, Quantum enhanced optomechanical magnetometry, Optica **5,** 850 (2018).

[32] B.-B. Li, G. Brawley, H. Greenall, S. Forstner, E. Sheridan, H. Rubinsztein-Dunlop, and W. P. Bowen, Ultrabroadband and sensitive cavity optomechanical magnetometry, Photonics Res. **8,** 1064 (2020).

[33] C. Zhang, T. Ling, S.-L. Chen, and L. J. Guo, Ultrabroad bandwidth and highly sensitive optical ultrasonic detector for photoacoustic imaging, ACS Photonics **1,** 1093 (2014).

[34] J. Sun, J.-W. Meng, S.-J. Tang, and C. Li, An encapsulated optical microsphere sensor for ultrasound detection and photoacoustic imaging, Sci. China Phys. Mech. Astron. **65,** 224211 (2022).

[35] H. Li, B. Dong, Z. Zhang, H. F. Zhang, and C. Sun, A transparent broadband ultrasonic detector based on an optical micro-ring resonator for photoacoustic microscopy, Sci. Rep. **4,** 4496 (2014).

[36] H. Li, B. Dong, X. Zhang, X. Shu, X. Chen, R. Hai, D. A. Czaplewski, H. F. Zhang, and C. Sun, Disposable ultrasound-sensing chronic cranial window by soft nanoimprinting lithography, Nat. Commun. **10,** 4277 (2019).

[37] J. A. Guggenheim, J. Li, T. J. Allen, R. J. Colchester, S. Noimark, O. Ogunlade, I. P. Parkin, I. Papakonstantinou, A. E. Desjardins, E. Z. Zhang, and P. C. Beard, Ultrasensitive plano-concave optical microresonators for ultrasound sensing, Nat. Photonics **11,** 714 (2017).

[38] R. Shnaiderman, G. Wissmeyer, O. Ulgen, Q. Mustafa, A. Chmyrov, and V. Ntziachristos, A submicrometre silicon-on-insulator resonator for ultrasound detection, Nature **585,** 372 (2020).

[39] W. J. Westerveld, M. Mahmud-Ul-Hasan, R. Shnaiderman, V. Ntziachristos, X. Rottenberg, S. Severi, and V. Rochus, Sensitive, small, broadband and scalable optomechanical ultrasound sensor in silicon photonics, Nat. Photonics **15,** 341 (2021).

[40] F. Monifi, B. Peng, S. K. Ozdemir, L. Ma, K. Maslov, L. V. Wang, and L. Yang, in *2013 IEEE Photonics Conference* (IEEE, Bellevue, WA, USA, 2013), p. 215.

[41] K. Huang and M. Hossein-Zadeh, Underwater acoustic signal detection and down-conversion using optomechanical resonance and oscillation, J. Lightwave Technol. **38,** 3789 (2020).

[42] M. V. Chistiakova and A. M. Armani, Photoelastic ultrasound detection using ultra-high-Q silica optical resonators, Opt. Express **22,** 28169 (2014).

[43] K. H. Kim, W. Luo, C. Zhang, C. Tian, L. J. Guo, X. Wang, and X. Fan, Air-coupled ultrasound detection using capillary-based optical ring resonators, Sci. Rep. **7,** 109 (2017).

[44] J. Pan, B. Zhang, Z. Liu, J. Zhao, Y. Feng, L. Wan, and Z. Li, Microbubble resonators combined with a digital optical frequency comb for high-precision air-coupled ultrasound detectors, Photonics Res. **8,** 303 (2020).

[45] J. Yang, T. Qin, F. Zhang, X. Chen, X. Jiang, and W. Wan, Multiphysical sensing of light, sound and microwave in a microcavity Brillouin laser, Nanophotonics **9,** 2915 (2020).

[46] S. Basiri-Esfahani, A. Armin, S. Forstner, and W. P. Bowen, Precision ultrasound sensing on a chip, Nat. Commun. **10,** 132 (2019).

[47] G. Wissmeyer, M. A. Pleitez, A. Rosenthal, and V. Ntziachristos, Looking at sound: Optoacoustics with all-optical ultrasound detection, Light Sci. Appl. **7,** 53 (2018).

[48] S. M. Leinders, W. J. Westerveld, J. Pozo, P. L. van Neer, B. Snyder, P. O'Brien, H. P. Urbach, N. de Jong, and M. D. Verweij, A sensitive optical micro-machined ultrasound sensor (OMUS) based on a silicon photonic ring resonator on an acoustical membrane, Sci. Rep. **5,** 14328 (2015).

[49] H. Quang Tri, P. Verboven, X. Yin, P. C. Struik, and B. M. Nicolai, A microscale model for combined CO_2 diffusion and photosynthesis in leaves, PLoS ONE **7,** e48376 (2012).

[50] G. Rousseau, A. Blouin, and J.-P. Monchalin, Non-contact photoacoustic tomography and ultrasonography for tissue imaging, Biomed. Opt. Express **3,** 16 (2012).

[51] W. P. Bowen and G. Milburn, *Quantum Optomechanics* (CRC Press, Boca Raton, 2016).

[52] D. K. Armani, T. J. Kippenberg, S. M. Spillane, and K. J. Vahala, Ultra-high-Q toroid microcavity on a chip, Nature **421,** 925 (2003).

[53] J. C. Knight, G. Cheung, F. Jacques, and T. A. Birks, Phase-matched excitation of whispering-gallery-mode resonances by a fiber taper, Opt. Lett. **22,** 1129 (1997).

[54] G. G. Stokes, On the theories of the internal friction in fluids in motion, and of the equilibrium and motion of elastic solids, Trans. Camb. Philos. Soc. **8,** 287 (1845).

[55] G. Kirchhoff, Ueber den Einfluss der Wärmeleitung in einem Gase auf die Schallbewegung (The effect of heat conduction in a gas on the movement of sound), Ann. Phys. **210,** 177 (1868).

[56] T. Carmon, H. Rokhsari, L. Yang, T. J. Kippenberg, and K. J. Vahala, Temporal Behavior of Radiation-Pressure-Induced Vibrations of an Optical Microcavity Phonon Mode, Phys. Rev. Lett. **94,** 223902 (2005).

[57] T. J. Kippenberg, H. Rokhsari, T. Carmon, A. Scherer, and K. J. Vahala, Analysis of Radiation-Pressure Induced Mechanical Oscillation of an Optical Microcavity, Phys. Rev. Lett. **95,** 033901 (2005).

[58] M. Bao, *Analysis and Design Principles of MEMS Devices* (Elsevier, Amsterdam, 2005).

[59] U. A. Javid, S. D. Rogers, A. Graf, and Q. Lin, Cavity optomechanical sensing in the nonlinear saturation limit, Laser Photonics Rev. **15**, 2100166 (2021).

[60] M.-A. Miri, G. D'Aguanno, and A. Alù, Optomechanical frequency combs, New J. Phys. **20**, 043013 (2018).

[61] M. Poot, K. Y. Fong, M. Bagheri, W. H. P. Pernice, and H. X. Tang, Backaction limits on self-sustained optomechanical oscillations, Phys. Rev. A **86**, 053826 (2012).

[62] P. Djorwe, J. Y. Effa, and S. G. Nana Engo, Multistability, staircases, and optical high-order sideband combs in optomechanics, J. Opt. Soc. Am. B **37**, A36 (2020).

[63] H. Xiong, L. Si, X. Lv, X. Yang, and Y. Wu, Review of cavity optomechanics in the weak-coupling regime: From linearization to intrinsic nonlinear interactions, Sci. China Phys. Mech. Astron. **58**, 1 (2015).

[64] C. Doolin, B. D. Hauer, P. H. Kim, A. J. R. MacDonald, H. Ramp, and J. P. Davis, Nonlinear optomechanics in the stationary regime, Phys.Rev. A **89**, 053838 (2014).

[65] L. Chang, S. Liu, and J. E. Bowers, Integrated optical frequency comb technologies, Nat. Photonics **16**, 95 (2022).

Correction: The third and fifth affiliations were inadvertently repeated, so the fifth affiliation was removed and the affiliation of the eight author was changed from 5 to 3. The postal code of the first affiliation contained an error and has been set right.